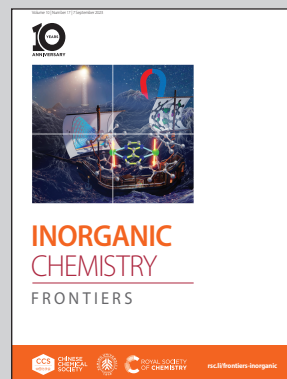


Showcasing research from Professor Haixin Chang's laboratory, School of Materials Science and Engineering, Huazhong University of Science and Technology, Wuhan, China.

"FeV-cofactor"-inspired bionic Fe-doped BiVO_4 photocatalyst decorated with few-layer 2D black phosphorus for efficient nitrogen reduction

In-built bionic FeV cofactor in Fe- BiVO_4 catalyst decorated with 2D black phosphorus can not only adsorb and activate N_2 molecules, but also promote carrier separation and transfer, thus improving photocatalytic nitrogen reduction performance.

As featured in:



See Shaonan Gu, Guofu Wang, Haixin Chang *et al.*, *Inorg. Chem. Front.*, 2023, 10, 5004.

Registered charity number: 207890

RESEARCH ARTICLE

View Article Online

View Journal | View Issue

Cite this: *Inorg. Chem. Front.*, 2023, **10**, 5004**"FeV-cofactor"-inspired bionic Fe-doped BiVO₄ photocatalyst decorated with few-layer 2D black phosphorus for efficient nitrogen reduction†**Hongda Li,^{a,c} Shuai Jian,^a Boran Tao,^{a,c} Guoxiao Xu,^a Baosheng Liu,^a Shaonan Gu,^{*b} Guofu Wang^{*a} and Haixin Chang^{id} ^{*c}

Drawing inspiration from the biological nitrogenase mechanism, bionic photocatalytic nitrogen fixation technology plays a significant role in activating nitrogen molecules and promoting the nitrogen reduction reaction. However, developing effective semiconductor photocatalysts remains a considerable challenge in the field of bionic nitrogen fixation. Herein, a novel bionic "FeV-cofactor" system for performing photocatalytic nitrogen reduction was proposed for the first time based on an Fe-doped BiVO₄ photocatalyst decorated with few-layer 2D black phosphorus (BP). As expected, Fe doping and BP decoration significantly improved the NH₃ yield of BiVO₄. With an NH₃ yield of 337.9 μmol g⁻¹ h⁻¹ (6.83 times that of BiVO₄), FeBiVO₄-0.05BP ranks among the top-performing nitrogen-fixing materials in oxide-based photocatalysts. DFT calculations show that N₂ molecules can be adsorbed and activated by Fe doping, thus forming the in-built bionic "FeV-cofactor". The experimental results further confirm that introducing a bionic "FeV-cofactor" system enhances the electron transfer between redox couples (V⁵⁺/V⁴⁺ & Fe³⁺/Fe²⁺) and N₂, thus improving the carrier separation efficiency. Oxygen vacancies coupled with V⁴⁺ ions also contribute to increasing light absorption. The 2D BP decoration plays a crucial role in the whole process of nitrogen reduction due to its exceptional electron transfer ability while increasing the active sites of the reaction.

Received 15th May 2023,
Accepted 20th July 2023
DOI: 10.1039/d3qi00895a

rsc.li/frontiers-inorganic

Introduction

Ammonia (NH₃) is a potential hydrogen energy carrier and an important feedstock in producing plastics, fertilizers, and other chemicals whose effects permeate all human lives.^{1,2} The Haber-Bosch process, currently used for the industrial production of NH₃, involves high-purity N₂ and H₂ reacting under extreme conditions (20–40 MPa, 400–600 °C), resulting in high energy consumption and CO₂ emissions.³ Exploring an environmentally friendly NH₃ production route is necessary to replace the traditional process.

In nature, diazotrophic bacteria and archaea reduce N₂ to NH₃ through nitrogenase-catalyzed reactions.⁴ Bionic nitrogen fixation has attracted significant attention due to its similarity to natural processes. Using abundant solar energy, bionic photocatalytic nitrogen fixation can achieve sustainable NH₃ synthesis under ambient conditions, which is both energy sustainable and environmentally friendly.^{5–7} Despite its potential, photocatalytic nitrogen fixation suffers from low conversion efficiency, mainly because the stable triple bond N≡N (941 kJ mol⁻¹) is difficult to be activated or cleaved under ambient conditions.⁸ Furthermore, semiconductor photocatalysts typically exhibit poor interfacial charge transfer and/or light absorption, limiting their applicability in charge- and energy-intensive nitrogen reduction reactions.⁹

Three different nitrogenases have similar characteristics and can be classified as the FeMo-cofactor, FeFe-cofactor, and FeV-cofactor based on the metallic composition of catalytic cofactors; the FeMo-cofactor is the most extensively studied.¹⁰ Consequently, FeMo-based bionic semiconductor photocatalysts for nitrogen reduction have attracted significant attention. Studies on FeMo-based bionic nitrogen-fixing photocatalysts such as MIL-88A (Fe/Mo)¹¹ and Fe-doped Bi₂MoO₆¹² have been conducted. Our previous research also suggested that

^aLiuzhou Key Laboratory for New Energy Vehicle Power Lithium Battery, School of Electronic Engineering, Guangxi University of Science and Technology, Liuzhou, 545006, China^bKey Laboratory of Fine Chemicals in Universities of Shandong, Jinan Engineering Laboratory for Multi-Scale Functional Materials, School of Chemistry and Chemical Engineering, Qilu University of Technology (Shandong Academy of Sciences), Jinan 250353, China^cQuantum-Nano Matter and Device Lab, State Key Laboratory of Material Processing and Die & Mould Technology, School of Materials Science and Engineering, Huazhong University of Science and Technology, Wuhan 430074, China†Electronic supplementary information (ESI) available. See DOI: <https://doi.org/10.1039/d3qi00895a>

constructing a bionic FeMo-cofactor effectively enhances the nitrogen reduction activity. The formation of a bionic “FeMo-cofactor” in Fe-doped MoTe_2 ¹³ and Fe/Mo bimetallic-coated $\text{Bi}_2\text{Mo}_{0.3}\text{W}_{0.7}\text{O}_6$ nanocrystals¹⁴ can effectively promote the separation and transfer of photoinduced carriers. However, despite structural similarities between the FeV-cofactor and FeMo-cofactor in nitrogenase, these variants exhibit different nitrogen reduction mechanisms,¹⁵ and it is unclear how different metal compositions affect catalytic performance and the possible mechanisms. Bionic catalytic cofactors in various forms also exhibit diverse reaction mechanisms. More importantly, the formation of bionic FeV-cofactor has not been reported in the field of semiconductor photocatalytic nitrogen reduction, leaving its relevant mechanisms unknown. Similarly, questions persist about which metal in the bionic FeV-cofactor sites are active for nitrogen reduction and whether bimetallic synergies between V and Fe sites may play a role.

BiVO_4 is a well-known semiconductor photocatalyst. The monoclinic form of BiVO_4 possesses a suitable band gap (2.3–2.4 eV) and an ideal electronic structure.^{16,17} It has been reported that BiVO_4 exhibits notable photocatalytic nitrogen fixation performance,^{18,19} and it is one of the ideal candidates for FeV-based bionic nitrogen-fixing photocatalysts. Furthermore, black phosphorus (BP), an emerging low-cost and highly efficient metal-free co-catalyst, has shown excellent assistant effects in photocatalytic nitrogen reduction,^{20–22} due to its excellent optical/electronic properties such as broad-spectrum light capture capability, high carrier mobility ($\sim 1000 \text{ cm}^2 \text{ V}^{-1} \text{ s}^{-1}$) and tunable band gap (0.3–2.0 eV).^{23–25} Herein, we present a novel bionic Fe-doped BiVO_4 photocatalyst decorated with BP for nitrogen reduction. By integrating DFT calculations and experimental results, we demonstrated that the inbuilt bionic “FeV-cofactor” not only adsorbed and activated N_2 molecules but also promoted electron transfer between redox couples ($\text{V}^{5+}/\text{V}^{4+}$ & $\text{Fe}^{3+}/\text{Fe}^{2+}$) and N_2 , thus improving the carrier separation efficiency. Oxygen vacancies coupled with V^{4+} ions also contribute to increasing light absorption. Simultaneously, 2D BP decoration plays a key role in the whole nitrogen reduction of bionic FeV cofactor photocatalysts due to its superior electron transfer ability while increasing the active sites of the reaction. This work provides an effective approach to designing bionic FeV-based inorganic semiconductor photocatalysts for nitrogen reduction.

Experimental section

Preparation of BiVO_4 and Fe-doped BiVO_4 (FeBiVO_4) samples

BiVO_4 and FeBiVO_4 samples were synthesized using a hydrothermal method. In the standard procedure, 0.970 g (2 mmol) of $\text{Bi}(\text{NO}_3)_3 \cdot 5\text{H}_2\text{O}$ and 0.234 g (2 mmol) of NH_4VO_3 were dissolved in 30 mL of HNO_3 solution (2 mol L^{-1}) and 30 mL of deionized water, respectively. The NH_4VO_3 solution was added dropwise to $\text{Bi}(\text{NO}_3)_3$ solution and stirred for 60 min. To synthesize 2 mol% Fe-doped BiVO_4 (FeBiVO_4) samples, 0.04 mmol

$\text{Fe}(\text{NO}_3)_3 \cdot 9\text{H}_2\text{O}$ was added into the above solution mixture. The pH value of the resulting solution was adjusted to 7 with NaOH (4 mol L^{-1}) and stirred for 60 min. Then, the final mixture was transferred into a 100 mL Teflon-lined stainless-steel autoclave and maintained at 200 °C for 18 h. After the reaction, the product was collected by filtration, washed three times with deionized water, and dried at 80 °C for 12 h.

Preparation of 2D black phosphorus (BP) nanosheets

Bulk BP was synthesized using a simple low-pressure transport route. 0.5 g of red phosphorus, 0.02 g of Sn, and 0.01 g of SnI_4 were sealed in a vacuum quartz tube. The quartz tube was heated to 650 °C at a rate of 2 °C min^{-1} and maintained at 650 °C for 5 h, then cooled to 500 °C at a cooling rate of 0.5 °C min^{-1} , and then cooled naturally to room temperature. BP single crystals were collected and stored in a glove box for subsequent use. 2D BP nanosheets were produced by liquid exfoliation of bulk BP.²⁶ Specifically, 30 mg of BP was dispersed in 100 mL of ethanol under Ar, and the suspension was ultrasonicated for 10 h. Finally, the stable suspension was centrifuged at 5000 rpm for 10 min to obtain nanosheets.

Preparation of BiVO_4/BP and $\text{FeBiVO}_4/\text{BP}$ heterojunctions

BiVO_4/BP and $\text{FeBiVO}_4/\text{BP}$ heterojunctions were synthesized using the electrostatic self-assembly method.²⁷ A specified amount of BP nanosheets and 100 mg of BiVO_4 or FeBiVO_4 were added into 100 mL of ethanol and sonicated for 120 min under Ar to obtain a stable homogeneous dispersion. The resulting products (BiVO_4/BP or $\text{FeBiVO}_4/\text{BP}$) were collected by centrifugation and vacuum-dried at 80 °C for 6 h. The composite heterojunction catalysts were obtained as follows: $\text{BiVO}_4/5 \text{ wt\%BP}$ ($\text{BiVO}_4\text{-}0.05\text{BP}$), $\text{FeBiVO}_4/2 \text{ wt\%BP}$ ($\text{FeBiVO}_4\text{-}0.02\text{BP}$), $\text{FeBiVO}_4/5 \text{ wt\%BP}$ ($\text{FeBiVO}_4\text{-}0.05\text{BP}$), and $\text{FeBiVO}_4/10 \text{ wt\%BP}$ ($\text{FeBiVO}_4\text{-}0.10\text{BP}$).

Characterization

Powder X-ray diffraction (XRD) patterns were detected using an XRD instrument (SmartLab SE, Rigaku, Japan) equipped with Cu K α radiation ($\lambda = 1.5418 \text{ \AA}$). The microstructure and morphology were characterized by field-emission scanning electron microscopy (FESEM; MIRA LMS, TESCAN, Czech Republic), transmission electron microscopy (TEM; JEM 2100F, JEOL, Japan), and atomic force microscopy (AFM; Dimension Icon, Bruker, Germany). The specific surface areas were measured using the Brunauer-Emmett-Teller (BET) method (ASAP2460, Micromeritics, USA). The actual contents of Bi, Fe, P, and V elements were collected using an inductively coupled plasma optical emission spectrometer (ICP-OES; Avio 200, PerkinElmer, USA). X-ray photoelectron spectroscopy (XPS) was carried out with an X-ray photoelectron spectrometer (K-Alpha, Thermo Scientific, USA). The UV-vis diffuse reflectance spectra (DRS) data were recorded using a UV-vis spectrophotometer (UV-3600i Plus, Shimadzu, Japan). Fluorescence lifetimes and apparent quantum efficiency (AQE) were determined using a steady-state/transient fluorescence spectrometer (FLS980, Edinburgh Instruments, UK) with an excitation laser

of 375 nm. Electron paramagnetic resonance (EPR) spectra were detected with an electron paramagnetic resonance spectrometer (Bruker A300, Bruker Corporation, Germany). Photoelectrochemical and the electrochemical impedance spectrum (EIS) measurements were conducted in a traditional three-electrode system using an electrochemical workstation (CHI 760E, Shanghai Chenhua, China), as described in our previous study.²⁸

Photocatalytic N₂ reduction evaluation

Photocatalytic nitrogen reduction reactions were conducted in a quartz reactor under the illumination of a 300 W xenon lamp with 420 nm cutoff filter. The sample (30 mg) was dispersed in 60 mL of ultrapure water (multiple distillations to remove NH₄⁺) at 25 °C. Before irradiation, the mixture was stirred in the dark under high-purity nitrogen (purity ≥99.999%, 100 mL min⁻¹) for 60 min to saturate the suspension with nitrogen. The lamp was then turned on, and 3 mL of the suspension was collected every 30 min for 2 h. The concentration of NH₄⁺ was determined by Nessler's reagent spectrophotometry (UH4150, Hitachi, Japan) and ion chromatography (Dionex Aquion RFIC, ThermoFisher, USA) equipped with a cation detector. An isotopic labeling experiment was conducted using ¹⁵N isotope-labeled N₂ by the photocatalytic nitrogen reduction reaction process. A nuclear magnetic resonance spectrometer (NMR, AVANCE III HD 500 M, Bruker, USA) was used to detect the characteristic peaks of ¹⁵NH₄⁺, and dimethyl sulfoxide was used to calibrate the chemical shifts of the ¹H NMR spectra. Besides, the pH of the aqueous solution was adjusted using 1 M H₂SO₄ or 1 M NaOH to explore the effect of pH on N₂ reduction activity.

Computational details

All calculations for BiVO₄ and FeBiVO₄ models were conducted within the spin-polarized DFT framework, as implemented in the DMol3 code available in Materials Studio.²⁹ The generalized gradient approximation (GGA) in the form of the Perdew–Wang (PW91) functional^{30,31} was used to describe the exchange-correlation term. Core electrons of the transition metal were replaced by effective nuclear potential pseudopotential (ECP), and the valence electron wave function set was chosen as double-numerical polarization (DNP). All geometries were fully optimized until the energy tolerance reached less than 2.0×10^{-5} Ha, the maximum displacement was less than 5.0×10^{-3} Å, and the convergence of force on each atom was 4.0×10^{-1} Ha Å⁻¹. The convergence criterion of the self-consistent field (SCF) is 10^{-6} Ha. Adsorption energy (E_b) is defined as the difference between the total energy of the adsorption systems (E_t), and the sum of the calculated surface energy (E_s) and N₂ energy (E_{N_2}):³²

$$E_b = E_t - (E_{N_2} + E_s) \quad (1)$$

The Gibbs free energy changes for each N₂ reduction step were calculated as follows:³³

$$\Delta G = \Delta ZPE + \Delta E - T\Delta S \quad (2)$$

where ΔZPE and ΔE are the calculated zero-point energy difference and total energy difference, respectively, and $T\Delta S$ is the entropy contribution at 298.15 K.

Results and discussion

Structure and chemical state

The XRD patterns (Fig. 1) show that the diffraction peaks of all samples align well with the standard card of BiVO₄ (JCPDS #14-0688), indicating the successful realization of the monoclinic phase of BiVO₄.^{34,35} For single Fe-doped samples (FeBiVO₄), no Fe-related crystalline phase is observed due to the low Fe content.³⁶ In addition, since Fe³⁺/Fe²⁺ ion radius (67 pm/78 pm) is less than Bi³⁺ ion radius (103 pm), the lattice parameters of BiVO₄ decrease after Fe³⁺/Fe²⁺ replaces Bi³⁺ (Table S1†), indicating that Fe ions partially replace Bi³⁺ and enter into the BiVO₄ lattice.¹³ For the BP-decorated samples, two new peaks appear at $2\theta = 16.8^\circ$ and 52.3° (lattice planes of (0 2 0) and (0 6 0)) and an overlapping peak appears at $2\theta = 34.2^\circ$ (lattice plane of (0 4 0)) due to the introduction of black phosphorus (BP) (JCPDS #67-1957).³⁷ The XRD intensities of BP peaks increase with the increasing amount of BP.

Fig. S1a–d† shows the SEM images of BiVO₄, FeBiVO₄, FeBiVO₄-0.05BP, and BiVO₄-0.05BP samples. It is evident that the ternary FeBiVO₄-0.05BP photocatalyst consists of FeBiVO₄ nanoparticles and BP nanosheets, and Fe doping has no effect on the morphology of the catalysts. Additionally, the thickness of the 2D BP nanosheets is about 4 nm, while the thickness of FeBiVO₄ particles is larger than 100 nm, as shown in Fig. 2. The ICP-OES analysis (Table S2†) shows that the real molarity of Fe and mass concentration of P is roughly consistent with the theoretical concentrations. In particular, the addition of BP nanosheets is conducive to increasing the BET surface areas of the catalytic system (Table S1†).

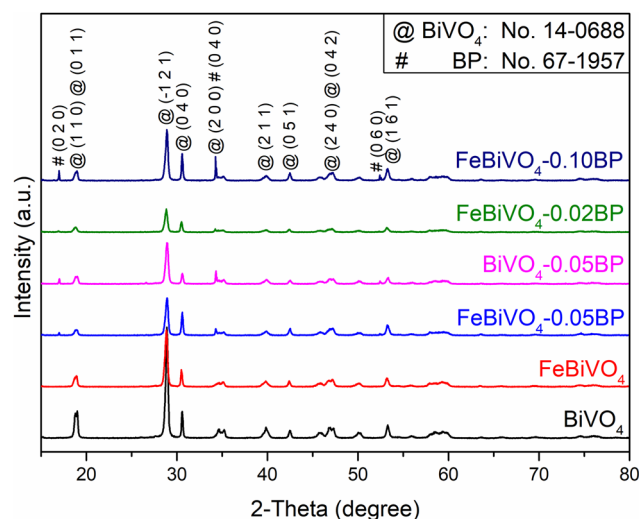


Fig. 1 XRD patterns of different samples: BiVO₄, FeBiVO₄, BiVO₄-0.05BP, FeBiVO₄-0.05BP, FeBiVO₄-0.02BP and FeBiVO₄-0.10BP.

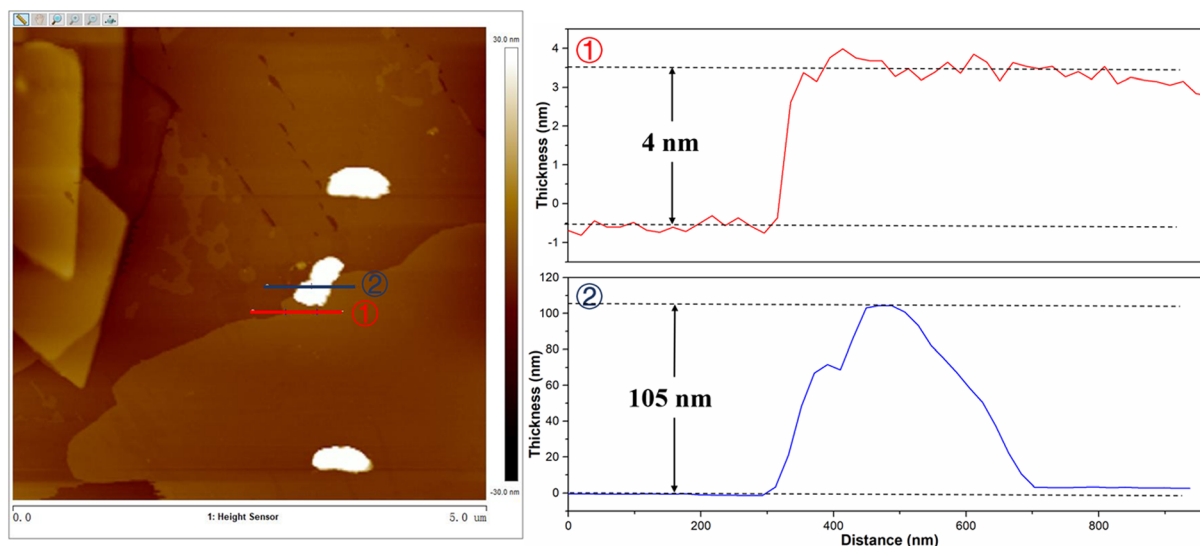


Fig. 2 AFM images of $\text{FeBiVO}_4\text{-0.05BP}$ (left) and the corresponding thickness distribution (right).

High-resolution TEM, high-angle annular dark-field scanning TEM (HAADF-STEM), and energy dispersive spectrometer (EDS) mapping analysis were carried out to reveal the heterogeneous structure and elemental distribution in the $\text{FeBiVO}_4\text{-0.05BP}$ samples (Fig. 3). The high-resolution TEM of $\text{FeBiVO}_4\text{-0.05BP}$ (Fig. 3b) shows interplanar spacings of 0.29, 0.47, and 0.31 nm, which matched with the (2 0 0), (1 1 0) and $(-1\ 2\ 1)$ planes of the monoclinic BiVO_4 , respectively. Fig. 3c–i displays the HAADF-STEM image and the corresponding EDS mapping. The result shows a uniform distribution of Bi, O, V, Fe, and P elements in the $\text{FeBiVO}_4\text{-0.05BP}$ sample, indicating that the Fe ions and BP nanosheets are evenly introduced into the catalytic system. These results fully confirm the successful formation of homogeneous-doped $\text{FeBiVO}_4\text{-0.05BP}$ heterojunction composites.

The XPS analysis provides information about the valence states and elemental composition of the BiVO_4 and $\text{FeBiVO}_4\text{-0.05BP}$ samples,³⁸ as shown in Fig. 4. The O XPS spectra (Fig. 4a) have two peaks at 530.2 and 532.9 eV, attributed to bound oxygen (O_L , Bi–O, and V–O) and adsorbed oxygen (O_{OH}) in BiVO_4 , respectively.³⁹ The O peak at 531.8 eV was attributed to the increased adsorption capacity of the catalyst surface by the introduction of oxygen vacancies (O_v) in $\text{FeBiVO}_4\text{-0.05BP}$,⁴⁰ indicating the oxygen vacancy formation due to Fe ion doping. Meanwhile, oxygen vacancies in BiVO_4 usually accompany the coupling formation of V^{4+} species.⁴¹ Fig. 4b shows the XPS spectra of V 2p, which contains two peaks with binding energies of 524.4 and 516.9 eV, respectively, ascribed to V 2p_{1/2} and V 2p_{3/2} of the V^{5+} cation. After Fe ion doping, a new peak at 515.0 eV can be assigned to the V^{4+} cation,⁴² which confirms the formation of a couple of oxygen vacancies and V^{4+} species in Fe-doped BiVO_4 . Furthermore, the XPS spectra of Bi are shifted by doping Fe ions, demonstrating that Fe is involved in the bonding of the BiVO_4 lattice⁴³ (Fig. S2†). Additionally, after Fe ions were introduced into the catalyst system, XPS peaks of

the $\text{Fe}^{3+}/\text{Fe}^{2+}$ couple could be observed in Fig. 4c. In detail, the binding energies of 728.8 eV (2p_{1/2}) and 713.5 eV (2p_{3/2}) are the peaks of the Fe^{3+} cation, while the binding energies of 724.0 eV (2p_{1/2}) and 710.4 eV (2p_{3/2}) belong to the Fe^{2+} cation. These results show that $\text{V}^{5+}/\text{V}^{4+}$ and $\text{Fe}^{3+}/\text{Fe}^{2+}$ redox couples are successfully introduced into BiVO_4 crystals by doping Fe ions. As for the XPS spectra of P 2p in $\text{FeBiVO}_4\text{-0.05BP}$, Fig. 4d displays two fitted peaks at 129.6 and 128.9 eV, respectively, ascribed to P 2p_{1/2} and P 2p_{3/2} of P^0 .⁴⁴ Moreover, a stronger PO_x peak is found in the XPS spectrum of the $\text{FeBiVO}_4\text{-0.05BP}$ sample, which is related to the oxidation of BP in $\text{FeBiVO}_4\text{-0.05BP}$ samples. An oxidation process is inevitable in BP-based materials.⁴⁵

Evaluation of the photocatalytic nitrogen reduction performance

The photocatalytic nitrogen reduction performance of the prepared samples under visible light is evaluated without an organic scavenger, as shown in Fig. 5a. The concentrations of N_2H_4 and NH_3 in the reaction solutions were simultaneously detected, but no N_2H_4 was observed. After 120 min of visible light irradiation, the NH_3 yield of pure BiVO_4 was $49.45\ \mu\text{mol g}^{-1}\ \text{h}^{-1}$. As expected, both Fe doping and BP decoration significantly enhanced the NH_3 yield of BiVO_4 . The NH_3 yield of $\text{FeBiVO}_4\text{-0.05BP}$ is $337.9\ \mu\text{mol g}^{-1}\ \text{h}^{-1}$, which is 6.83 times that of BiVO_4 . The results obtained by cationic exchange chromatography are almost identical (Fig. S3†). Compared to other photocatalysts, the $\text{FeBiVO}_4\text{-0.05BP}$ photocatalyst exhibited excellent nitrogen reduction activity (Table S3†). NH_3 production of $\text{FeBiVO}_4\text{-0.10BP}$ ($265.9\ \mu\text{mol g}^{-1}\ \text{h}^{-1}$) decreased when the concentration of BP decoration was increased to 10%, possibly due to excessive BP being the recombination centers of photoinduced carriers. Moreover, the $\text{FeBiVO}_4\text{-0.05BP}$ photocatalytic system did not produce NH_3 when only high-purity Ar flows continuously, which means that N_2 is the

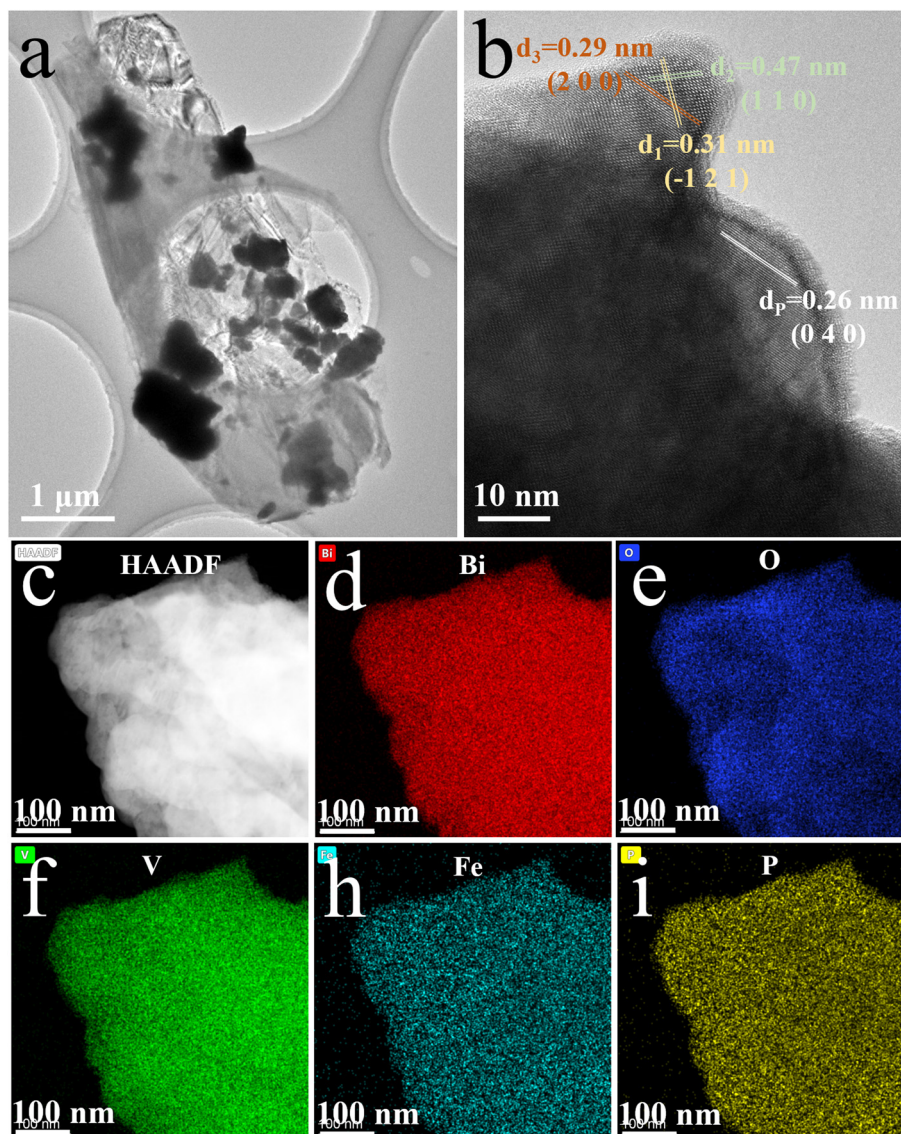


Fig. 3 (a) TEM and (b) High-resolution TEM images of $\text{FeBiVO}_4\text{-0.05BP}$; (c) HAADF-STEM image and corresponding EDS mapping: (d) Bi, (e) O, (f) V, (h) Fe, (i) P.

only nitrogen source to produce NH_3 . The photocatalytic nitrogen reduction stability of $\text{FeBiVO}_4\text{-0.05BP}$ is evaluated by seven cycles, as shown in Fig. 5b. The results indicate that the nitrogen reduction activity and structure of $\text{FeBiVO}_4\text{-0.05BP}$ are relatively stable in multiple cycles (Fig. S4†).

To further confirm the accuracy of NH_3 generation from N_2 , an isotope labeling test was performed to examine the reaction solution of $\text{FeBiVO}_4\text{-0.05BP}$ (Fig. 5c). Generally, the ^1H NMR spectra of the $^{15}\text{NH}_4^+$ standard sample displays a pair of coupled peaks.⁴⁶ The characteristic peaks of $^{15}\text{NH}_4^+$ are detected using the ^1H NMR spectrum when the feeding gas is $^{15}\text{N}_2$, indicating that the N element of NH_3 comes from the feed gas N_2 .

Fig. 5d shows the effect of pH values of the reaction solution on NH_3 yield investigated. When $\text{pH} = 7$, the reduction

performance of N_2 is the best, while the increase or decrease of pH value will lead to the decrease of photocatalytic N_2 reduction activities. Under acidic conditions, an increase in H^+ concentration leads to decreased water oxidation. However, under alkaline conditions, although the oxidation of water was improved, the produced NH_4^+ was being oxidized faster, thus reducing the production of NH_3 .⁴⁷

Mechanism of improved photocatalytic activity

To explore the mechanism of Fe doping or 2D BP decoration in regulating the nitrogen reduction reaction one by one, first, theoretical calculations were conducted on the mechanism of Fe doping on BiVO_4 (Fig. 6). There are three main reaction pathways in the process of photocatalytic NH_3 synthesis,

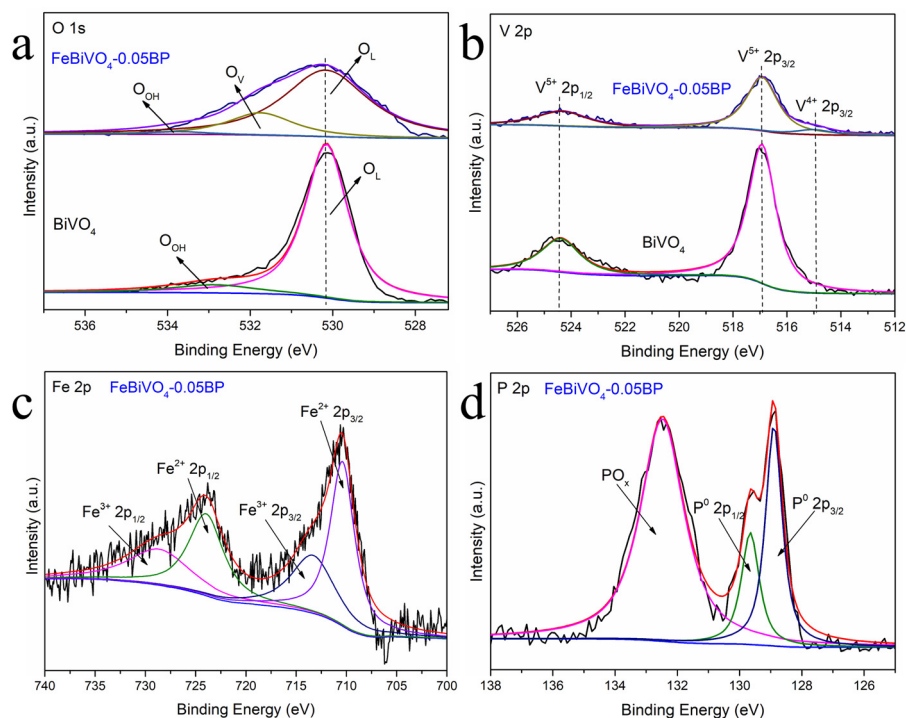


Fig. 4 High-resolution XPS of (a) O 1s and (b) V 2p for BiVO_4 and $\text{FeBiVO}_4\text{-0.05BP}$, high-resolution XPS of (c) Fe 2p and (d) P 2p for $\text{FeBiVO}_4\text{-0.05BP}$.

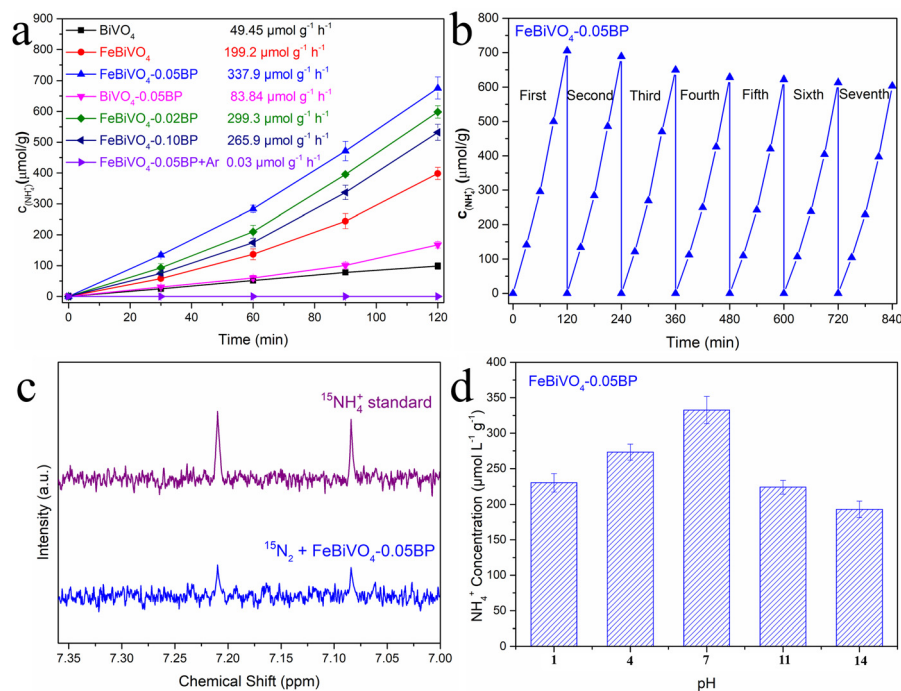


Fig. 5 (a) Photocatalytic N_2 reduction of BiVO_4 , FeBiVO_4 , $\text{BiVO}_4\text{-0.05BP}$, $\text{FeBiVO}_4\text{-0.05BP}$, $\text{FeBiVO}_4\text{-0.02BP}$ and $\text{FeBiVO}_4\text{-0.10BP}$ under visible light irradiation. (b) Stability test for the nitrogen reduction of the $\text{FeBiVO}_4\text{-0.05BP}$ photocatalyst. (c) ^{15}H NMR spectra qualitative isotope labeling test of $\text{FeBiVO}_4\text{-0.05BP}$. (d) The NH_4^+ yield of the $\text{FeBiVO}_4\text{-0.05BP}$ sample under different pH conditions after 2 h.

namely the distal reaction pathway, alternate reaction pathway, and enzymatic reaction pathway.⁴⁸ The distal mechanism was considered the most potential reaction pathway in the BiVO_4

system.¹⁸ The optimized structures of the reaction intermediate for nitrogen reduction over BiVO_4 and FeBiVO_4 by a distal mechanism are presented in Fig. 6a and b. Moreover, it has

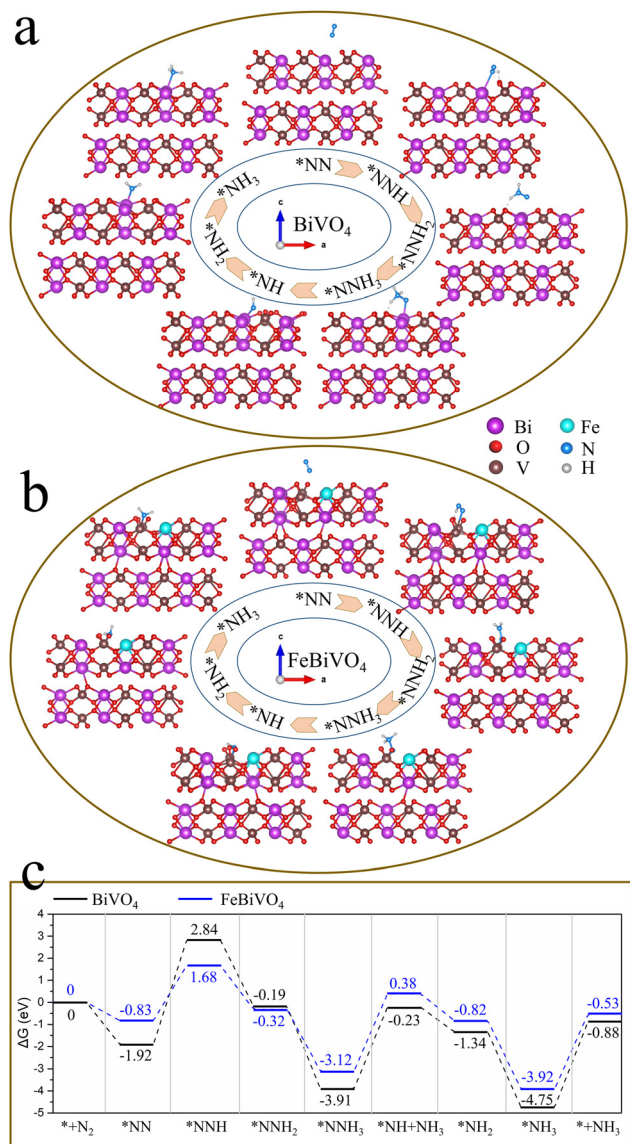
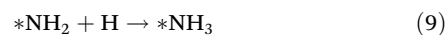
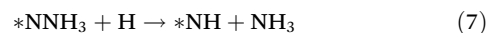
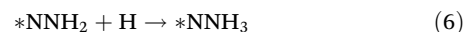
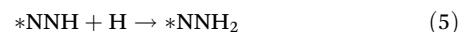


Fig. 6 Optimized structures of reaction intermediates in a distal mechanism: (a) BiVO₄ and (b) FeBiVO₄; (c) Gibbs free energy profiles of nitrogen reduction over BiVO₄ and FeBiVO₄ catalysts by a distal mechanism.

been reported that N₂ molecules can only be adsorbed on the (0 4 0) plane of BiVO₄.¹⁸ Herein, we focus on the nitrogen reduction reaction occurring on the (0 4 0) plane of BiVO₄ and FeBiVO₄, respectively. When BiVO₄ is involved in the nitrogen reduction reaction, the adsorption and reduction of N₂ molecules occur at the Bi sites, while the V sites are almost not directly involved. During the nitrogen reduction reaction of FeBiVO₄, the adsorption and reduction of N₂ at the active sites are mainly related to the V sites, which may be due to the bionic effect of FeV formed by Fe doping. This effect can promote the adsorption and activation of N₂ molecules, and the formed V⁵⁺/V⁴⁺ and Fe³⁺/Fe²⁺ redox couples can promote the continuous transfer of multiple electrons/protons (Fig. S5†).

Fig. 6c shows the Gibbs free energy profiles of nitrogen reduction over BiVO₄ and FeBiVO₄ catalysts by a distal mechanism. For the nitrogen reduction reaction of BiVO₄, three steps are involved in the increase of the Gibbs free energy. The first step is the hydrogenation of the adsorbed N₂ molecules (eqn (4)), increasing the free energy by 4.76 eV. The second step is the release of the first NH₃ (eqn (7)), and the free energy is increased by 3.68 eV. The third step is the release of the second NH₃ (eqn (10)), and the free energy is increased by 3.87 eV. Except for these three steps, the remaining nitrogen reduction processes are exergonic. It can be found that the rate-determining step of the nitrogen reduction reaction by BiVO₄ is the generation of the *NNH intermediate (eqn (4)). Although the increase in Gibbs free energy also has three steps for the nitrogen reduction reaction of FeBiVO₄, the rate-determining step changed to the generation of the first NH₃ (eqn (7)), and it also has a lower ΔG value of 3.50 eV than that of BiVO₄ (3.68 eV). The DFT results showed that the design of the bionic FeV made the hydrogenation of N₂ (eqn (4)) no longer a decisive step in the catalytic system, indicating that the construction of FeV active centers is conducive to the activation and hydrogenation of N₂ molecules, thus effectively accelerating the conversion of N₂ to NH₃. Each basic reaction step can be written as follows. The corresponding equations for the change in Gibbs free energy are as follows.



Subsequently, the above calculation results were verified experimentally, and the synergistic effect of Fe doping and 2D BP decoration was further explored. Fe doping and BP decoration greatly improved the photocatalytic activity of BiVO₄. This improvement is usually due to the increased specific surface area, enhanced charge separation, and improved light absorption. As mentioned above, Fe doping hardly affects the specific surface area of the BiVO₄ catalysts, while BP can significantly increase the specific surface area of the BiVO₄ and FeBiVO₄ catalysts by promoting the dispersion of the BiVO₄ nanoparticles (Fig. S1 and Table S2†), thus increasing the number of active sites required for the reaction.

More importantly, photocurrent response experiments were performed and time-resolved photoluminescence (PL) spectra were obtained to evaluate the photoinduced charge carrier generation, separation, and transfer efficiency in the BiVO₄ and FeBiVO₄-0.05BP photocatalysts.⁴⁹ As shown in Fig. 7a, the

photocurrent intensities of Fe- or V-modified samples are higher than that of pure BiVO_4 , and FeBiVO_4 -0.05BP showed the strongest photocurrent intensity, indicating that both Fe doping and BP decoration can greatly promote the generation and transfer of photoinduced charge carriers. Furthermore, electrochemical impedance spectroscopy (EIS) was applied to study the influence of the Fe doping and BP decoration on the impedance property of BiVO_4 (Fig. 7b). The FeBiVO_4 -0.05BP curve corresponds to the smallest arc radius, which indicates that the photo-generated carriers are subjected to the least resistance during the transfer process. Compared with BP decoration, the effect of Fe doping on impedance is significantly greater, indicating that Fe doping may be the direct cause of promoting continuous transfer of multiple electrons/protons by the formed $\text{V}^{5+}/\text{V}^{4+}$ and $\text{Fe}^{3+}/\text{Fe}^{2+}$.

As illustrated in Fig. S6,[†] the formula of $\tau_{\text{avg.}} = \frac{\sum A_i \tau_i^2}{\sum A_i \tau_i}$ is used to calculate the average fluorescence lifetime, where the decay in fluorescence intensity (I) with time (t) is fitted by a phenomenological double exponential:⁵⁰

$$I = A_1 \exp\left(-\frac{t - t_0}{\tau_1}\right) + A_2 \exp\left(-\frac{t - t_0}{\tau_2}\right) \quad (11)$$

The fluorescence life of FeBiVO_4 -0.05BP (8.29 ns) is about 3.5 times that of BiVO_4 (2.37 ns). In addition, the apparent quantum efficiency (AQE) of the BiVO_4 and FeBiVO_4 -0.05BP samples is measured under 420 and 460 nm monochromatic

light with intensities of 4.72 and 5.65 mW cm^{-2} , respectively. The AQE is calculated by the following formula:⁵¹

$$\text{AQE} = \frac{N_{\text{NH}_3}}{N_p} = \frac{6 \times \text{the number of evolved NH}_3 \text{ molecules}}{\text{the number of incident photons}} \times 100\% \quad (12)$$

The NH_3 yields of BiVO_4 and FeBiVO_4 -0.05BP were measured after 2 h of light irradiation. The AQE of FeBiVO_4 -0.05BP reached 2.53% at 420 nm and 1.22% at 460 nm, respectively, which are significantly higher than that of BiVO_4 (0.85% at 420 nm and 0.52% at 460 nm).

These results demonstrate that the inbuilt bionic FeV cofactor not only adsorbs and activates N_2 molecules but also promotes the electron transfer between redox couples ($\text{V}^{5+}/\text{V}^{4+}$ & $\text{Fe}^{3+}/\text{Fe}^{2+}$) and N_2 , thus improving the efficiency of carrier separation. 2D BP decoration not only increases the active sites of the nitrogen reduction reaction but also contributes to accelerating the electron transport of the catalytic system.

Electron paramagnetic resonance (EPR) was used to detect the sample's structural characteristics and oxygen vacancies (OV). As shown in Fig. 7c, almost no signal is observed for BiVO_4 at $g = 2.001$, while two strong characteristic peaks appeared for both FeBiVO_4 and FeBiVO_4 -0.05BP, which are typical of oxygen vacancies.⁵² It is further confirmed that the catalytic system generated coupled V^{4+} and O_v after the Fe doping, which is consistent with the results of XPS. The appearance of O_v can change the electronic structure of the semiconductor and generate subbands.⁵³ XPS valence band

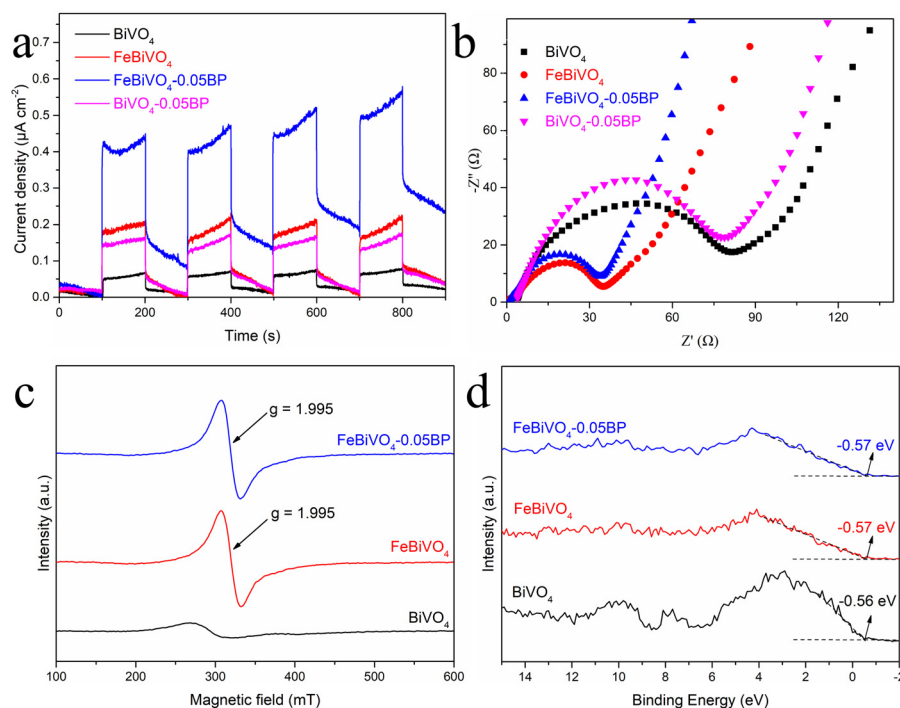


Fig. 7 (a) Photocurrent response and (b) electrochemical impedance spectroscopy (EIS) tests of BiVO_4 , FeBiVO_4 , BiVO_4 -0.05BP and FeBiVO_4 -0.05BP; (c) EPR spectra and (d) XPS valence state spectra of BiVO_4 , FeBiVO_4 and FeBiVO_4 -0.05BP.

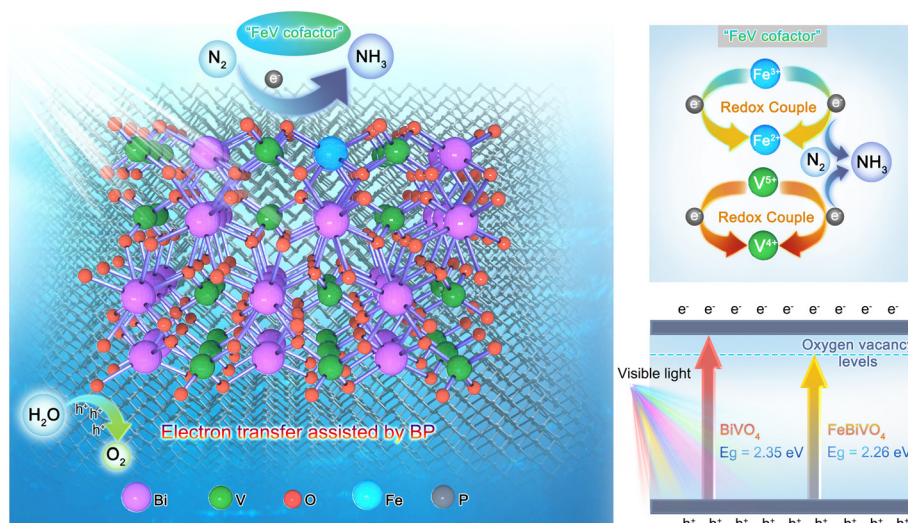
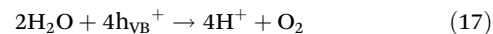
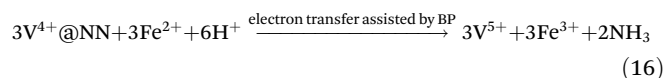
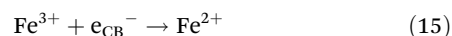
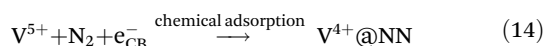
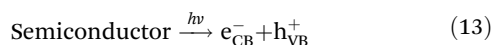


Fig. 8 Schematic diagram of the nitrogen reduction mechanisms over the FeBiVO₄-0.05BP photocatalyst.

spectra are used to characterize the approximate valence band (VB) location in the photocatalysts, as shown in Fig. 7d. The VB values of BiVO₄, FeBiVO₄, and FeBiVO₄-0.05BP are almost the same, indicating that Fe doping and BP decoration had little effect on the VB of BiVO₄. The DRS results show that Fe doping has the most obvious effect on the band gap (Fig. S7†), indicating that the O_v caused by Fe doping moves down the conduction band (CB) of the semiconductor catalytic system to a certain extent, thus leading to a decrease in the band gap when the VB value remains unchanged.

Based on the above results, the internal mechanisms of Fe doping and 2D BP decoration in regulating photocatalytic nitrogen reduction are summarized, as shown in Fig. 8. Fe doping induces lattice distortion to form the Fe³⁺/Fe²⁺ and V⁵⁺/V⁴⁺ redox couples ("FeV-cofactor"), which not only adsorbs and activates N₂ molecules but also promotes the electron transfer between "FeV-cofactor" and N₂; appropriate 2D BP decoration can not only increase the active sites of the reaction but also facilitate the rapid electron transfer in the process of nitrogen reduction. In classical photocatalysis, electrons on VB are excited and transferred to the conduction band (CB) to obtain photoinduced electrons (e_{CB}⁻) and form holes in VB (h_{VB}⁺), as shown in eqn (13). N₂ molecules are adsorbed onto the V sites of the (0 4 0) plane in BiVO₄, then capture e_{CB}⁻ and combine with the V-O bond to form a stable adsorption structure (V⁴⁺@NN), as shown in eqn (14). At the same time, Fe³⁺ captures e_{CB}⁻ to form Fe²⁺ (eqn (15)). With the assistance of BP, the reductive V⁴⁺@NN and the equally reductive Fe²⁺ react with the free H⁺ to form NH₃ (eqn (16)). At this point, h_{VB}⁺ can react directly with H₂O molecules to form O₂ (eqn (17)).



Moreover, the formation of O_v can form defect levels below the CB, which can accommodate low-energy electrons excited by low-energy light;⁵⁴ and e_{CB}⁻ in the CB can also be further transferred to the O_v levels, significantly inhibiting the recombination of charge carriers. Furthermore, with the introduction of O_v, V atoms with lower coordination and high spin polarization become more favorable active sites.⁵⁵

Conclusion

In summary, a novel bionic "FeV-cofactor" system for photocatalytic nitrogen reduction was designed and prepared for the first time, using Fe-doped BiVO₄ that is decorated with 2D BP (FeBiVO₄-0.05BP). DFT calculations show that N₂ molecules can be adsorbed and activated by Fe doping, forming the in-built bionic "FeV-cofactor". The experimental results further confirms that the bionic "FeV-cofactor" system enhances electron transfer between redox couples (V⁵⁺/V⁴⁺ & Fe³⁺/Fe²⁺) and N₂, thus improving the carrier separation efficiency. Oxygen vacancies coupled with V⁴⁺ ions also contribute to increasing light absorption. 2D BP decoration not only increases the active sites of the nitrogen reduction reaction but also contributes to accelerating the electron transport within the catalytic system. Thus, the FeBiVO₄-0.05BP catalyst exhibits superior photocatalytic nitrogen reduction activity with an NH₃ yield of 337.9 μmol g⁻¹ h⁻¹ (6.83 times that of BiVO₄), making it one of the best nitrogen-fixing materials among oxide-based photocatalysts.

Conflicts of interest

The authors declare no competing financial interest.

Acknowledgements

This work was financially supported by the Natural Science Foundation of Guangxi Province (No. 2021GXNSFAA220108, 2020GXNSFBA297122), Specific Research Project of Guangxi for Research Bases and Talents (No. AD20297134), National Key Research and Development Program (No. 2022YFEO134600, 2021YFA0715404), Guangxi Key Research and Development Program (No. 2021AB05083) and Science, Education and Industry Integration of Basic Research Projects of Qilu University of Technology (Grant No. 2022PY062). The authors would like to thank Yunyun Zou from Shiyanjia Lab (<https://www.shiyanjia.com>) for the SEM, TEM and XPS studies.

References

- 1 J. G. Chen, R. M. Crooks, L. C. Seefeldt, K. L. Bren, R. M. Bullock, M. Y. Darensbourg, P. L. Holland, B. Hoffman, M. J. Janik, A. K. Jones, M. G. Kanatzidis, P. King, K. M. Lancaster, S. V. Lyman, P. Pfaff, W. F. Schneider and R. R. Schrock, Beyond fossil fuel-driven nitrogen transformations, *Science*, 2018, **360**, eaar6611.
- 2 J. P. Zehr and D. G. Capone, Changing perspectives in marine nitrogen fixation, *Science*, 2020, **368**, eaay9514.
- 3 Y. Luo, G. F. Chen, L. Ding, X. Chen, L. X. Ding and H. Wang, Efficient electrocatalytic N₂ fixation with MXene under ambient conditions, *Joule*, 2019, **3**, 279–289.
- 4 D. E. Canfield, A. N. Glazer and P. G. Falkowski, The evolution and future of Earth's nitrogen cycle, *Science*, 2010, **330**, 192–196.
- 5 C.-L. Chen, H.-Y. Wang, J.-P. Li, L.-S. Long, X.-J. Kong and L.-S. Zheng, Assembling lanthanide–transition metal clusters on TiO₂ for photocatalytic nitrogen fixation, *Inorg. Chem. Front.*, 2022, **9**, 2862–2868.
- 6 H. Li, C. Li, B. Tao, S. Gu, Y. Xie, H. Wu, G. Zhang, G. Wang, W. Zhang and H. Chang, Two-Dimensional Metal Telluride Atomic Crystals (2D MTACs): Preparation, Physical Properties and Applications, *Adv. Funct. Mater.*, 2021, **31**, 2010901.
- 7 G. Dong, X. Huang and Y. Bi, Anchoring Black Phosphorus Quantum Dots on Fe-Doped W₁₈O₄₉ Nanowires for Efficient Photocatalytic Nitrogen Fixation, *Angew. Chem., Int. Ed.*, 2022, **134**, e202204271.
- 8 K. A. Brown, D. F. Harris, M. B. Wilker, A. Rasmussen, N. Khadka, H. Hamby, S. Keable, G. Dukovic, J. W. Peters, L. C. Seefeldt and P. W. King, Light-driven dinitrogen reduction catalyzed by a CdS: nitrogenase MoFe protein biohybrid, *Science*, 2016, **352**, 448–450.
- 9 H. L. Jia, A. X. Du, H. Zhang, J. H. Yang, R. B. Jiang, J. F. Wang and C. Y. Zhang, Site-selective growth of crystal-line ceria with oxygen vacancies on gold nanocrystals for near-infrared nitrogen photofixation, *J. Am. Chem. Soc.*, 2019, **141**, 5083–5086.
- 10 S. L. Foster, S. I. P. Bakovic, R. D. Duda, S. Maheshwari, R. D. Milton, S. D. Minter, M. J. Janik, J. N. Renner and L. F. Greenlee, Catalysts for nitrogen reduction to ammonia, *Nat. Catal.*, 2018, **1**, 490–500.
- 11 W. Wang, J. Qu, C. Li, L. Guo, X. Fang, G. Chen and J. Duan, “MoFe cofactor” inspired iron mesh-based MIL88A(Fe/Mo) for bionic photocatalytic nitrogen fixation, *Mol. Catal.*, 2022, **532**, 112730.
- 12 Q. Meng, C. Lv, J. Sun, W. Hong, W. Xing, L. Qiang, G. Chen and X. Jin, High-efficiency Fe-Mediated Bi₂MoO₆ nitrogen-fixing photocatalyst: Reduced surface work function and ameliorated surface reaction, *Appl. Catal., B*, 2019, **256**, 117781.
- 13 H. Li, S. Gu, Z. Sun, F. Guo, Y. Xie, B. Tao, X. He, W. Zhang and H. Chang, In-built bionic “MoFe-cofactor” in Fe-doped two-dimensional MoTe₂ nanosheets for boosting the photocatalytic nitrogen reduction performance, *J. Mater. Chem. A*, 2020, **8**, 13038–13048.
- 14 H. Li, H. Deng, S. Gu, C. Li, B. Tao, S. Chen, X. He, G. Wang, W. Zhang and H. Chang, Engineering of bionic Fe/Mo bimetallic for boosting the photocatalytic nitrogen reduction performance, *J. Colloid Interface Sci.*, 2022, **607**, 1625–1632.
- 15 B. Benediktsson and R. Bjornsson, Quantum Mechanics/Molecular Mechanics Study of Resting-State Vanadium Nitrogenase: Molecular and Electronic Structure of the Iron–Vanadium Cofactor, *Inorg. Chem.*, 2020, **59**, 11514–11527.
- 16 Y. Qi, J. Zhang, Y. Kong, Y. Zhao, S. Chen, D. Li, W. Liu, Y. Chen, T. Xie, J. Cui, C. Li, K. Domen and F. Zhang, Unraveling of cocatalysts photodeposited selectively on facets of BiVO₄ to boost solar water splitting, *Nat. Commun.*, 2022, **13**, 484.
- 17 D. Philo, S. Luo, C. He, Q. Wang, F. Ichihara, L. Jia, M. Oshikiri, H. Pang, Y. Wang, S. Li, G. Yang, X. Ren, H. Lin and J. Ye, Lattice Distortion Engineering over Ultrathin Monoclinic BiVO₄ Nanoflakes Triggering AQE up to 69.4% in Visible-Light-Driven Water Oxidation, *Adv. Funct. Mater.*, 2022, **32**, 2206811.
- 18 G. Zhang, Y. Meng, B. Xie, Z. Ni, H. Lu and S. Xia, Precise location and regulation of active sites for highly efficient photocatalytic synthesis of ammonia by facet-dependent BiVO₄ single crystals, *Appl. Catal., B*, 2021, **296**, 120379.
- 19 S. Shao, J. Zhang, L. Li, Y. Qin, Z.-Q. Liu and T. Wang, Visible-light-driven photocatalytic N₂ fixation to nitrates by 2D/2D ultrathin BiVO₄ nanosheet/rGO nanocomposites, *Chem. Commun.*, 2022, **58**, 2184.
- 20 Z.-K. Shen, Y.-J. Yuan, P. Wang, W. Bai, L. Pei, S. Wu, Z.-T. Yu and Z. Zou, Few-Layer Black Phosphorus Nanosheets: A Metal-Free Cocatalyst for Photocatalytic Nitrogen Fixation, *ACS Appl. Mater. Interfaces*, 2020, **12**, 17343–17352.

- 21 H. Li, C. Li, H. Zhao, B. Tao and G. Wang, Two-Dimensional Black Phosphorus: Preparation, Passivation and Lithium-Ion Battery Applications, *Molecules*, 2022, **27**, 5845.
- 22 P. Qiu, C. Xu, N. Zhou, H. Chen and F. Jiang, Metal-free black phosphorus nanosheets-decorated graphitic carbon nitride nanosheets with CeP bonds for excellent photocatalytic nitrogen fixation, *Appl. Catal., B*, 2018, **221**, 27–35.
- 23 J. Pei, J. Yang, T. Yildirim, H. Zhang and Y. Lu, Many-Body Complexes in 2D Semiconductors, *Adv. Mater.*, 2019, **31**, 1706945.
- 24 J. He, L. Tao, H. Zhang, B. Zhou and J. Li, Emerging 2D materials beyond graphene for ultrashort pulse generation in fiber lasers, *Nanoscale*, 2019, **11**, 2577–2593.
- 25 S. Guo, Y. Zhang, Y. Ge, S. Zhang, H. Zeng and H. Zhang, 2D V-V Binary Materials, *Adv. Mater.*, 2019, **31**, 1902352.
- 26 M. C. Stan, J. von Zamory, S. Passerini, T. Nilges and M. Winter, Puzzling out the origin of the electrochemical activity of black P as a negative electrode material for lithium-ion batteries, *J. Mater. Chem. A*, 2013, **1**, 5293–5300.
- 27 C. Chen, J. Hu, X. Yang, T. Yang, J. Qu, C. Guo and C. M. Li, Ambient-Stable Black Phosphorus-Based 2D/2D S-Scheme Heterojunction for Efficient Photocatalytic CO₂ Reduction to Syngas, *ACS Appl. Mater. Interfaces*, 2021, **13**, 20162–20173.
- 28 H. Zhou, Y. Liu, L. Zhang, H. Li, H. Liu and W. Li, Transition metal-doped amorphous molybdenum sulfide/graphene ternary cocatalysts for excellent photocatalytic hydrogen evolution: Synergistic effect of transition metal and graphene, *J. Colloid Interface Sci.*, 2019, **533**, 287–296.
- 29 B. Delley, An-electron numerical method for solving the local density functional for polyatomic molecules, *Chem. Phys.*, 1990, **92**, 508–517.
- 30 S. J. Xia, L. Fang, Y. Meng, X. Q. Zhang, L. Y. Zhang, C. Yang and Z. M. Ni, Water-gas shift reaction catalyzed by layered double hydroxides supported Au–Ni/Cu/Pt bimetallic alloys, *Appl. Catal., B*, 2020, **227**, 118949.
- 31 J. P. Perdew, K. Burke and M. Ernzerhof, Generalized gradient approximation made simple, *Phys. Rev. Lett.*, 1996, **77**, 3865–3868.
- 32 F. L. Hirshfeld, Bonded-atom fragments for describing molecular charge densities, *Theor. Chim. Acta*, 1977, **44**, 129–138.
- 33 Z. Guo, S. Qiu, H. Li, Y. Xu, S. J. Langford and C. Sun, Electrocatalytic Nitrogen Reduction Performance of Si-doped 2D Nanosheets of Boron Nitride Evaluated via Density Functional Theory, *ChemCatChem*, 2021, **13**, 1239–1245.
- 34 Y. Peng, J. Cai, Y. Shi, H. Jiang and G. Li, Thin p-type NiO nanosheet modified peanut-shaped monoclinic BiVO₄ for enhanced charge separation and photocatalytic activities, *Catal. Sci. Technol.*, 2022, **12**, 5162–5170.
- 35 S. Chen, D. L. Huang, P. Xu, X. M. Gong, W. J. Xue, L. Lei, R. Deng, J. Li and Z. H. Li, Facet-engineered surface and interface design of monoclinic scheelite bismuth vanadate for enhanced photocatalytic performance, *ACS Catal.*, 2020, **10**, 1024–1059.
- 36 S. Gu, W. Li, Y. Bian, F. Wang, H. Li and X. Liu, Highly-Visible-Light Photocatalytic Performance Derived from a Lanthanide Self-Redox Cycle in Ln₂O₃/BiVO₄ (Ln: Sm, Eu, Tb) Redox Heterojunction, *J. Phys. Chem. C*, 2016, **120**, 19242–19251.
- 37 M. Zhu, S. Kim, L. Mao, M. Fujitsuka, J. Zhang, X. Wang and T. Majima, Metal-Free Photocatalyst for H₂ Evolution in Visible to Near-Infrared Region: Black Phosphorus/Graphitic Carbon Nitride, *J. Am. Chem. Soc.*, 2017, **139**, 13234–13242.
- 38 Y. Li, L. Wang, F. Zhang, W. Zhang, G. Shao and P. Zhang, Detecting and Quantifying Wavelength-Dependent Electrons Transfer in Heterostructure Catalyst via In Situ Irradiation XPS, *Adv. Sci.*, 2023, **10**, 2205020.
- 39 L. Wang, M. Li, S. Wang, T. Zhang, F. Li and L. Xu, Enhanced photocatalytic nitrogen fixation in BiVO₄: constructing oxygen vacancies and promoting electron transfer through Ohmic contact, *New J. Chem.*, 2021, **45**, 22234–22242.
- 40 R. Shen, Y. Liu, H. Zhang, S. Liu, H. Wei, H. Yuan, H. Wen, X. Wu, S. Mehdi, T. Liu, J. Jiang, E. Liang and B. Li, Coupling oxygen vacancy and hetero-phase junction for boosting catalytic activity of Pd toward hydrogen generation, *Appl. Catal., B*, 2023, **328**, 122484.
- 41 N. österbacka and J. Wiktor, Influence of Oxygen Vacancies on the Structure of BiVO₄, *J. Phys. Chem. C*, 2021, **125**, 1200–1207.
- 42 S. Bakhtiarnia, S. Sheibani, A. Nadi, E. Aubry, H. Sun, P. Briois and M. A. P. Yazdi, Preparation of sputter-deposited Cu-doped BiVO₄ nanoporous thin films comprised of amorphous/crystalline heterostructure as enhanced visible-light photocatalyst, *Appl. Surf. Sci.*, 2023, **608**, 155248.
- 43 H. Li, H. Zhao, C. Li, B. Li, B. Tao, S. Gu, G. Wang and H. Chang, Redox regulation of photocatalytic nitrogen reduction reaction by gadolinium doping in two-dimensional bismuth molybdate nanosheets, *Appl. Surf. Sci.*, 2022, **600**, 154105.
- 44 J. Hu, D. Chen, Z. Mo, N. Li, Q. Xu, H. Li, J. He, H. Xu and J. Lu, Z-scheme 2D/2D heterojunction of black phosphorus/monolayer Bi₂WO₆ nanosheets with enhanced photocatalytic activities, *Angew. Chem., Int. Ed.*, 2019, **58**, 2073–2077.
- 45 T. Zhang, Y. Wan, H. Xie, Y. Mu, P. Du, D. Wang, X. Wu, H. Ji and L. Wan, Degradation chemistry and stabilization of exfoliated few-layer black phosphorus in water, *J. Am. Chem. Soc.*, 2018, **140**, 7561–7567.
- 46 X. Li, T. Li, Y. Ma, Q. Wei, W. Qiu, H. Guo, X. Shi, P. Zhang, A. M. Asiri, L. Chen, B. Tang and X. Sun, Boosted Electrocatalytic N₂ Reduction to NH₃ by Defect-Rich MoS₂ Nanoflower, *Adv. Energy Mater.*, 2018, **8**, 1801357.
- 47 Z. Zhao, S. Hong, C. Yan, C. Choi, Y. Jung, Y. Liu, Sh. Liu, X. Li, J. Qiu and Z. Sun, Efficient visible-light driven N₂ fixation over two-dimensional Sb/TiO₂ composites, *Chem. Commun.*, 2019, **55**, 7171–7174.

- 48 W. C. Xu, G. L. Fan, J. L. Chen, J. H. Li, L. Zhang, S. L. Zhu, X. C. Su, F. Y. Cheng and J. Chen, Nanoporous palladium hydride for electrocatalytic N_2 reduction under ambient conditions, *Angew. Chem., Int. Ed.*, 2020, **59**, 3511–3516.
- 49 C. Ren, W. Li, H. Li, X. Liu, Y. Liu, X. Li, C. Lin and H. Zhou, Ultrasmall Pt nanoclusters deposited on europium oxide: A newly active photocatalyst for visible-light-driven photocatalytic hydrogen evolution, *Appl. Surf. Sci.*, 2019, **480**, 96–104.
- 50 H. Ben, G. Yan, H. Liu, C. Ling, Y. Fan and X. Zhang, Local spatial polarization induced efficient charge separation of squaraine-linked COF for enhanced photocatalytic performance, *Adv. Funct. Mater.*, 2022, **32**, 2104519.
- 51 Y. Bai, L. Ye, T. Chen, L. i. Wang, X. Shi, X. Zhang and D. Chen, Facet-dependent photocatalytic N_2 fixation of bismuth-rich Bi_5O_7I nanosheets, *ACS Appl. Mater. Interfaces*, 2016, **8**, 27661–27668.
- 52 H. Li, W. Li, S. Gu, F. Wang, X. Liu and C. Ren, Forming Oxygen Vacancies Inside in Lutetium-doped Bi_2MoO_6 Nanosheets for Enhanced Visible-Light Photocatalytic Activity, *Mol. Catal.*, 2017, **433**, 301–312.
- 53 L. Wang, M. Li, S. Wang, T. Zhang, F. Li and L. Xu, Enhanced photocatalytic nitrogen fixation in $BiVO_4$: constructing oxygen vacancies and promoting electron transfer through Ohmic contact, *New J. Chem.*, 2021, **45**, 22234.
- 54 J. R. Ran, T. Y. Ma, G. P. Gao, X. W. Du and S. Z. Qiao, Porous P-doped graphitic carbon nitride nanosheets for synergistically enhanced visible-light photocatalytic H_2 production, *Energy Environ. Sci.*, 2015, **8**, 3708–3717.
- 55 J. X. Yao, D. Bao, Q. Zhang, M. M. Shi, Y. Wang, R. Gao, J. M. Yan and Q. Jiang, Tailoring Oxygen Vacancies of $BiVO_4$ toward Highly Efficient Noble-Metal-Free Electrocatalyst for Artificial N_2 Fixation under Ambient Conditions, *Small Methods*, 2019, **3**, 1800333.